RESEARCH ARTICLE

NANO · MICRO small
www.small-journal.com

A Self-Amplifying Photodynamic Biomedicine for Cascade Immune Activation Against Triple-Negative Breast Cancer

Xianquan Feng, Yan Zhang, Wanjing Lin, Jing Li, Fei Wu, Qingyu Lu, Hongtao Song, Hao Zhang, Fenghua Lan,* and Jun Lu**

The efficacy of immunotherapy in triple-negative breast cancer (TNBC) is significantly hindered by its low immunogenicity and immunosuppressive tumor microenvironment. Non-invasive photodynamic therapy (PDT) is increasingly recognized as a potential immunotherapeutic stimulant in the treatment of TNBC. However, photodynamic immunotherapy is constrained by tumor hypoxia and excessive inflammation suppression during the course of treatment. Herein, a simple and efficacious biomedicine is formulated to overcome adverse influences by amplifying photodynamic immunotherapy, thereby stimulating the systemic immune response. Specifically, the approach targeted tumor delivery by employing specific agents such as the photosensitizer (verteporfin), the hypoxic ameliorator (atovaquone), and the cyclooxygenase-2/prostaglandin E2 (COX-2/PGE2) signaling blocker (celecoxib). More importantly, the biomedicine effectively ameliorated hypoxia and inhibited COX-2/PGE2 signaling, thereby amplifying PDT-induced immunogenic cell death. This, in turn, enhanced the efficacy of photodynamic immunotherapy and triggered a robust immune response cascade. Notably, the self-amplifying photodynamic biomedicine significantly inhibited primary tumors, distal tumors, lung metastases, and post-operative recurrence while maintaining high biocompatibility. To sum up, the work provides a viable cascade stimulation approach and an efficient biomedical nanoplatform, offering a novel strategy for photodynamic immunotherapy of TNBC in the clinic.

1. Introduction

Triple-negative breast cancer (TNBC) is the most aggressive and metastatic subtype, characterized by limited therapeutic options, a grim prognosis, and high mortality rates.[1] At present, surgical resection and chemotherapy exhibit limitations in terms of both safety and effectiveness, leading to restricted clinical efficacy.[2] Immunotherapy has garnered significant attention in recent years for its ability to impede tumor cells through the activation of the body's immune system.[3] However, the low immunogenicity and highly immunosuppressive tumor microenvironment in TNBC contribute to poor response rates.[4] Immune checkpoint inhibitors, while acknowledged for their significant cost and limited applicability to specific patient populations, are impractical for widespread public benefit.[5] Consequently, there is a need to devise an effective strategy aimed at optimizing the host immune response.

The immunosuppressive tumor microenvironment (TME) is a major factor contributing to the low immunogenicity of TNBC, immune system suppression, and immune evasion.[6] Many factors reportedly affect the initiation and infiltration of cytotoxic T-lymphocytes (CTLs) into tumor tissues, such as lack of tumor immunogenicity, insufficient presentation of tumor antigens, and large hypoxic areas of the tumor, which can lead to the escape of tumor cells from the host immune system. Inducing immunogenic cell death (ICD), releasing tumor-associated antigens, and enhancing the immunogenicity of dead tumor cells through chemotherapy,[7] photodynamic therapy (PDT),[8] and photothermal therapy[9] is a novel means of tumor immunotherapy. These antigens can be further presented to dendritic cells (DCs), which, in turn, contribute to DC maturation and elicit a systemic immune response. In addition, the presence of a biologically active substance, prostaglandin E2 (PGE2), aberrantly expressed in tumor tissues, is associated with cancer progression and survival.[10] Two independent studies concurrently found that PGE2-EP2/EP4 inhibits CTL function and promotes immune escape by interfering with the interleukin-2 signaling pathway.[11] Thus, inhibiting PGE2 activity modulates changes in the immune cell population and is also a means of enhancing

X. Feng, F. Lan, J. Lu
Fujian Provincial Key Laboratory of Transplant Biology
Laboratory of Basic Medicine
Fuzong Clinical College of Fujian Medical University (900th Hospital of the Joint Logistics Support Force)
Fuzhou 350025, China
E-mail: fhlan@mail.fjmu.edu.cn; junlu.heather@xmu.edu.cn

Y. Zhang
Department of Oncology
Fuzong Clinical College of Fujian Medical University (900th Hospital of the Joint Logistics Support Force)
Fuzhou 350025, China

W. Lin, J. Li, F. Wu, Q. Lu, H. Song, H. Zhang
Department of Pharmacy
Fuzong Clinical College of Fujian Medical University (900th Hospital of the Joint Logistics Support Force)
Fuzhou 350025, China
E-mail: zh0922@fjmu.edu.cn

The ORCID identification number(s) for the author(s) of this article can be found under https://doi.org/10.1002/smll.202410214

DOI: 10.1002/smll.202410214

immunotherapy. Overall, improving the immunosuppressive TME through multiple strategies contributes to the enhancement of the anti-tumor immune response in TNBC.

Photodynamic therapy, as an emerging treatment, is minimally invasive, highly selective, and has low side effects for TNBC.[12] Photosensitizers produce reactive oxygen species (ROS) under laser irradiation, which not only damages tumor cells through powerful oxidation, but also releases tumor debris, which can increase tumor immunogenicity and has the potential to initiate anti-tumor immunity.[8,13] However, PDT requires oxygen consumption,[14] and the rapid proliferation of tumor cells also consumes oxygen,[15] further reducing PDT's efficacy. To date, tumor hypoxia can be mitigated either by direct oxygen supplementation or by reducing oxygen consumption.[16] Directly supplied oxygen is rapidly consumed by tumor cells or PDT while reducing oxygen consumption appears to be a more long-lasting approach to alleviate tumor hypoxia. Cellular oxygen consumption during respiration is primarily generated through mitochondria-related oxidative phosphorylation processes,[17] and atovaquone (ATO), an active inhibitor of mitochondrial respiratory chain complex III, has been used in combination with photosensitizers to improve PDT efficacy.[18] In addition, the PDT process induces the upregulation of tumor cyclooxygenase-2 (COX-2) expression, which promotes the secretion of PGE2, a key component in the formation of the tumor's immunosuppressive microenvironment, and can reduce the efficacy of photodynamic immunotherapy.[19] Some studies have combined chlorin e6 with celecoxib (CXB) to compensate for PDT's limitations and improve the immunosuppressive microenvironment.[20] Currently, few reports of combine the improvement of hypoxia and blockade of COX-2/PGE2 signaling to enhance photodynamic immunotherapy. Another significant challenge is how to co-deliver drugs to enhance photodynamic immunotherapy.

Inefficient drug delivery, differing physicochemical properties, and disparate delivery targets are all barriers to co-delivery, often leading to poor drug pharmacokinetics, in vivo distribution, and co-administration efficacy.[21] Therefore, constructing a drug co-delivery system based on nanotechnology is crucial to achieving synergistic pharmacological effects in tumor cells. With the development of nanotechnology, nanoparticles, liposomes, polymeric micelles, polymer-drug conjugates, and other nano-formulations have emerged.[22] Polymer-drug conjugates increase the solubility of hydrophobic drugs and protect them from degradation.[23] Liposomes can co-load drugs with widely differing physicochemical properties, but they risk drug leakage.[24] Some nanomedicine carriers have entered clinical trials or are used for disease diagnosis and treatment, such as the Food and Drug Administration (FDA)-approved albumin-bound paclitaxel nanoparticle (Abraxane), doxorubicin (Doxil), daunorubicin (DaunoXome) and so on.[25] Among these, human serum albumin (HSA), as a nanocarrier with multiple surface modification sites and hydrophobic structural domains, offers unique advantages such as good biocompatibility, strong drug binding ability, and degradability.[26] In addition, albumin-binding receptor-mediated enhancement of tumor uptake efficiency and enhanced permeability and retention (EPR) effects allow for enhanced tumor targeting and penetration.[27] Therefore, a nano-delivery system constructed based on HSA as a carrier is expected to address the challenge of co-delivering insoluble drugs to the tumor region.

In summary, a self-amplifying nanoplatform was rationally engineered to amplify positive outcomes and counteract negative effects, aiming to optimize photodynamic immunotherapy. As illustrated in **Scheme 1**, the intricately engineered co-delivery nanoplatform comprises a photosensitizer (verteporfin, VER), a hypoxic regulator (ATO), and an anti-inflammatory drug (CXB). Specifically, ATO ameliorates the hypoxic, immunosuppressive microenvironment and enhances VER-induced PDT, thereby augmenting tumor immunogenicity. Moreover, CXB targets the inflammatory COX-2/PGE2 pathway, thus alleviating the inflammation-associated immunosuppression induced by PGE2 upregulation during photodynamic immunotherapy. Furthermore, these strategies can synergistically amplify photodynamic immunotherapy to generate a durable immune memory effect, thereby effectively suppressing TNBC metastasis and recurrence. Our work likely contributes to ameliorating the immunosuppressed microenvironment in TNBC, thereby enhancing patients' responsiveness to immunotherapy.

2. Results and Discussion

2.1. Fabrication and Characterization of VCA NPs

To amplify the efficacy of VER-mediated photodynamic therapy, a formulation was developed by co-loading ATO (the oxygen deficiency regulator) and CXB (COX-2/PGE2 signal inhibitor) within HSA as a vehicle. Interestingly, the solutions of HSA and CXB appeared colorless and clear, while ATO exhibited a yellow hue, VER demonstrated a green color, and VCA NPs showed a yellow-green hue, which was attributed to the inherent properties of the drugs (Figure S1, Supporting Information). Notably, the Tyndall effect was apparent in the VCA NPs solutions (Figure S2, Supporting Information), confirming the presence of nanoparticles in the solution. Furthermore, VCA NPs exhibited a spherical morphology as shown by transmission electron microscopy (TEM). Dynamic light scattering (DLS) indicated that the size of VCA NPs was 144.2 nm, consistent with the TEM findings (**Figure 1A**). The nanoparticles exhibited an ideal uniform particle size distribution, as evidenced by their low polymer dispersity index (PDI) (0.1161) value. Subsequently, DLS was used to further characterize the positive and negative charges of the nanoparticles in aqueous solution. The VCA NPs were negatively charged with a zeta potential of −11.02 mV (Figure 1B), possibly due to the presence of acidic groups in the drug. Furthermore, UV–vis spectroscopy indicated the presence of characteristic absorption peaks of HSA, CXB, ATO, and VER in the VCA NPs (Figure 1C). The above results collectively confirmed that the nanoparticles have been successfully constructed.

The successfully constructed VCA NPs in water, PBS, saline, and 1640 medium with 10% fetal bovine serum (FBS) showed minimal alterations in particle size and PDI over a 7-day period (Figure S3, Supporting Information), indicating the stability of the synthesized nanoparticles. This indicated that albumin-constructed nanoparticles have the potential to enhance the stability of VER, ATO, and CXB, making them more suitable for in vivo applications. The encapsulation efficiencies

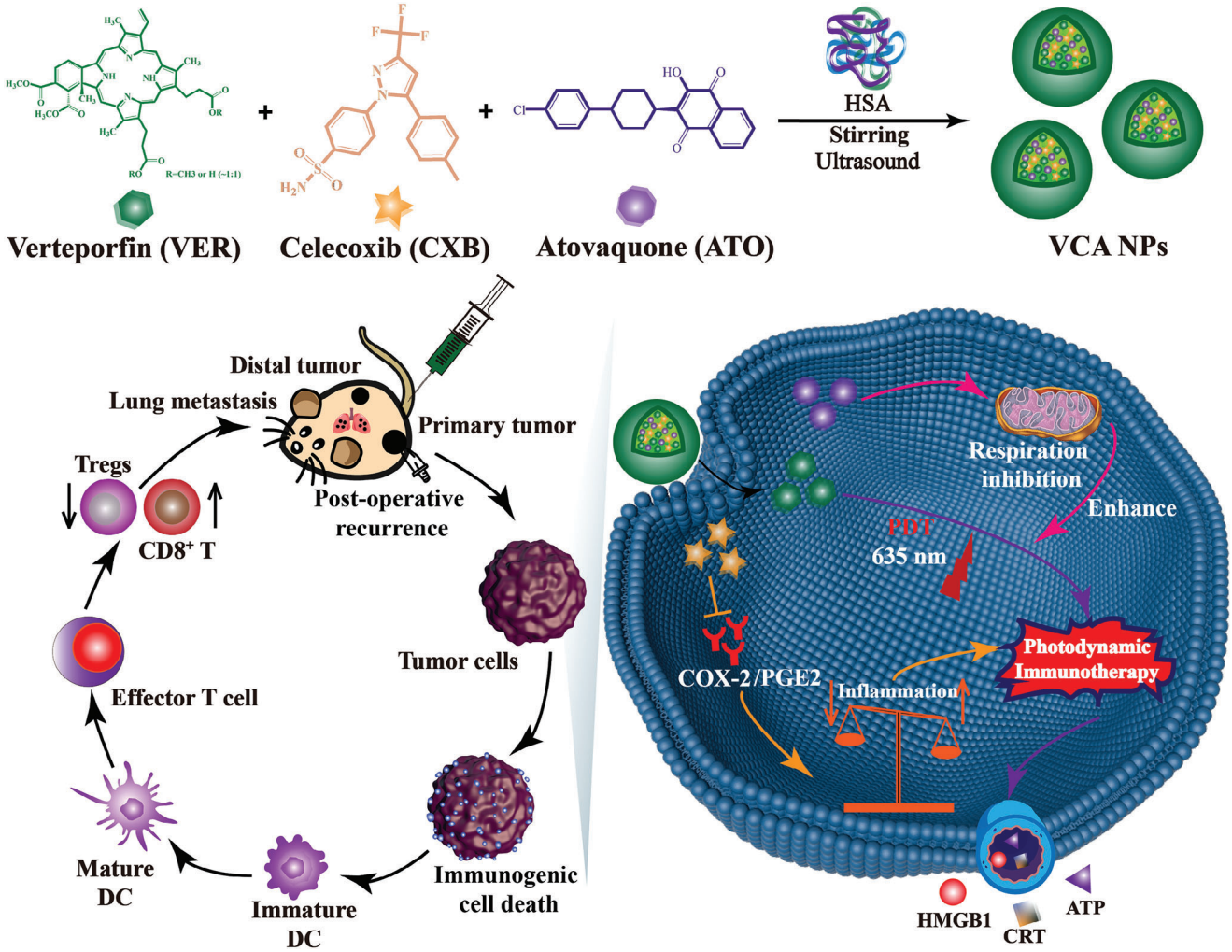

Scheme 1. Schematic illustration of VCA NPs-mediated photodynamic immunotherapy, demonstrating the cascade immune activation triggered by alleviating hypoxia and inhibiting COX-2/PGE2 signaling, thereby enhancing photodynamic therapy.

of VER, ATO, and CXB in VCA NPs were 84.07%, 82.95%, and 85.97%, respectively, as determined by high-performance liquid chromatography (HPLC) analysis. These findings indicated that albumin, as a drug delivery system, shows considerable promise, attributed to its immense capacity for drug loading. This capability may be attributed to the hydrophobic pockets of albumin.[28] Due to the presence of the carrier, the loading capacities of VER, ATO, and CXB in VCA NPs were 3.04%, 5.98%, and 6.22%, respectively. Subsequently, lyophilized formulations of VCA NPs were prepared by screening for lyophilization protectants, with 1% mannitol and 1% sucrose selected as the chosen protectants. The results indicated that the lyophilized formulations appeared as a full yellow-green powder, with minimal alteration in the particle size observed before and after lyophilization (Figure 1D). The aforementioned results confirmed that this method facilitated the long-term storage of lyophilized powder, making it suitable for market application.

2.2. Anti-Tumor Efficacy In Vitro

The cellular uptake behavior of the VCA NPs was examined by incubating the biomedicine for varying durations, showing a time-dependent increase in fluorescence within 4T1 cells (Figure S4, Supporting Information). Subsequently, the in vitro cytotoxicity of VCA NPs was evaluated using the MTT assay. VCA NPs exhibited a significant decrease in the viability of 4T1 cells compared to free CXB, ATO, and VER (Figure 1E). The impact of free VER and VCA NPs on 4T1 cells was studied in the absence of dark toxicity associated with VER. Cellular phototoxicity was more pronounced in the VCA NPs group when exposed to irradiation at a power density of 0.5 mW cm^{-2} for 10 min (Figure 1F), highlighting the enhanced cellular effectiveness of the biomedicine.

Live cells were identified by green fluorescence, while dead cells were distinguished by red fluorescence, and their status was examined using fluorescence microscopy. As shown in **Figure** 2A, no significant presence of dead cells was observed

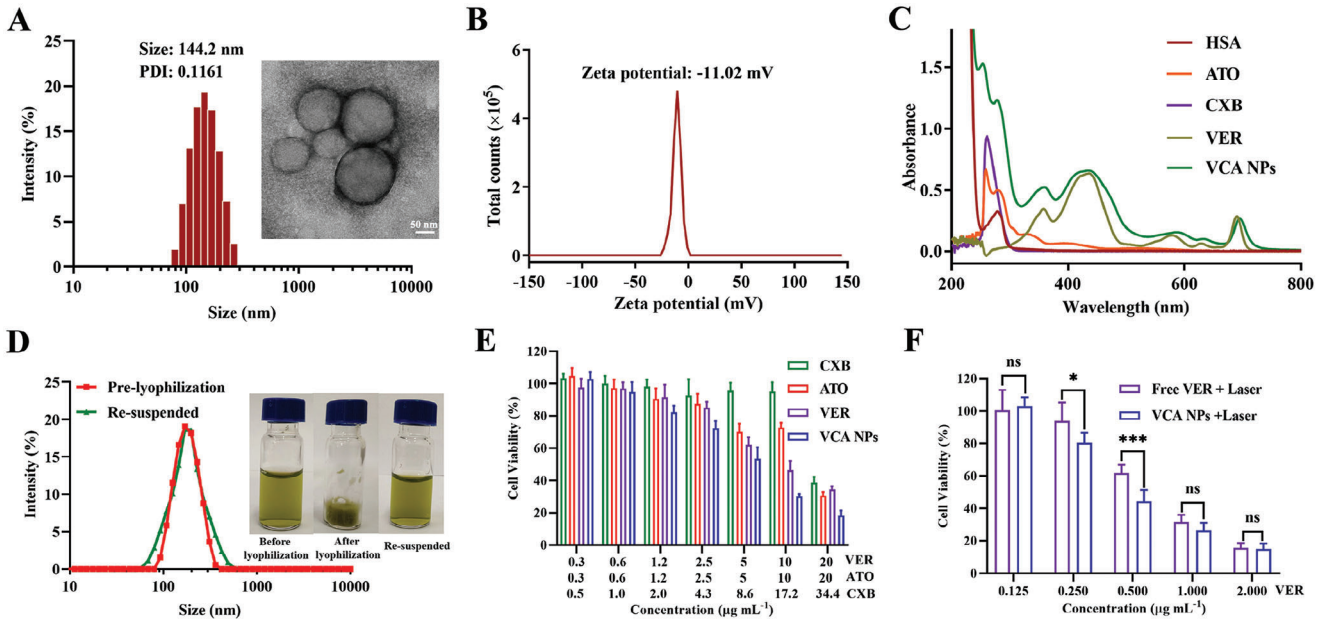

Figure 1. Characterization and cytotoxicity assessment of VCA NPs. (A) The size distribution and TEM images of VCA NPs, scale bar: 50 nm. (B) The zeta potential of VCA NPs determined via DLS. (C) UV–vis absorption spectra of HSA (human serum albumin), ATO (atovaquone), CXB (celecoxib), VER (verteporfin), and VCA NPs. (D) The changes in particle size pre- and post-reconstitution as well as lyophilized morphology. (E) The cytotoxicity assay of CXB, ATO, VER, and VCA NPs, $n = 6$. (F) The cytotoxic effects of photodynamic therapy mediated by free VER and VCA NPs, $n = 6$. The data are presented as mean ± SD, $^{*}p < 0.05$, $^{***}p < 0.001$.

in the PBS, CXB, and ATO groups; however, the laser-irradiated group (VER and VCA NPs) displayed extensive areas of cell death, with the highest abundance of dead cells found in the VCA NPs plus laser group. This outcome suggests a potential enhancement of VER-mediated phototoxicity by the other drugs. The results of the apoptosis assay indicated that the groups treated with VER plus laser and VCA NPs plus laser exhibited the highest levels of apoptosis, which were significantly greater than those observed in the remaining groups (Figure 2B). This finding further substantiates that the combined therapy leads to a more potent pro-apoptotic effect. Photodynamic therapy triggers apoptotic necrosis in tumor cells, probably attributed to the generation of ROS by photosensitizers upon exposure to laser irradiation.[29] We next investigated the potential synergistic enhancement of ROS production in tumor cells through the combination of VER-based photodynamic therapy with CXB and ATO. Tumor cell-derived ROS were detected by the 2′,7′-Dichlorodihydrofluorescein diacetate (DCFH-DA) probe, with the VCA NPs plus laser group exhibiting the highest intensity of green fluorescence, suggesting enhanced ROS production. (Figure 2C). This phenomenon may arise from ATO's ability to augment the effectiveness of VER-mediated photodynamic therapy.

Moreover, drawing inspiration from successful photodynamic therapy outcomes, we explored the ability of PDT to elicit an ICD response. The expression levels of high-mobility group box 1 (HMGB1) and calreticulin (CRT) in 4T1 cells, along with the substantial adenosine triphosphate (ATP) release, serve as crucial biomarkers indicating ICD response and as mechanisms to stimulate the immune microenvironment, ultimately enhancing the efficacy of immunotherapy.[30] Immunofluorescence staining for CRT by confocal laser scanning microscopy (CLSM) was conducted on 4T1 cells post-treatment, revealing intensified green immunofluorescence specifically in the VCA NPs plus laser group compared to the others, suggesting a relocation of CRT in the tumor cells (Figure 2D). Consistent findings were observed in the flow-through quantification analysis (Figure S5, Supporting Information), indicating the effective induction of ICD by the cells. Immediately afterward, the HMGB1 assay was conducted following the CRT staining protocol. The outcomes from both fluorescence microscopy and flow cytometry corroborated the efficient release of HMGB1 by the 4T1 cells in the VCA NPs plus laser group, providing additional confirmation of the VCA NPs' ability to induce ICD (Figure 2E; Figure S6, Supporting Information). Additionally, the highest ATP signal intensity was detected in the cells treated with VCA NPs plus laser, as depicted in Figure 2F, indicating a substantial release of ATP by the 4T1 cells. Overall, these results validated that PDT using VCA NPs triggered the ICD cascade in tumor cells, thereby boosting the host's anti-tumor immune response.

Most importantly, the activation of the immune system was notably enhanced in the VCA NPs plus laser group compared to the group that underwent laser irradiation alone. This enhancement may be attributed to the presence of ATO and CXB. The oxygen levels inside and outside the cell maintain a dynamic equilibrium. Therefore, the dissolved oxygen levels in the culture medium were measured with a dissolved oxygen meter, providing an indirect assessment of the oxygen content within the cell membrane. According to Figure 2G, the level of dissolved oxygen in the medium of the atovaquone-containing group (ATO and VCA NPs) markedly exceeded that of the other groups, suggesting a reduced rate of oxygen consumption. Further, the

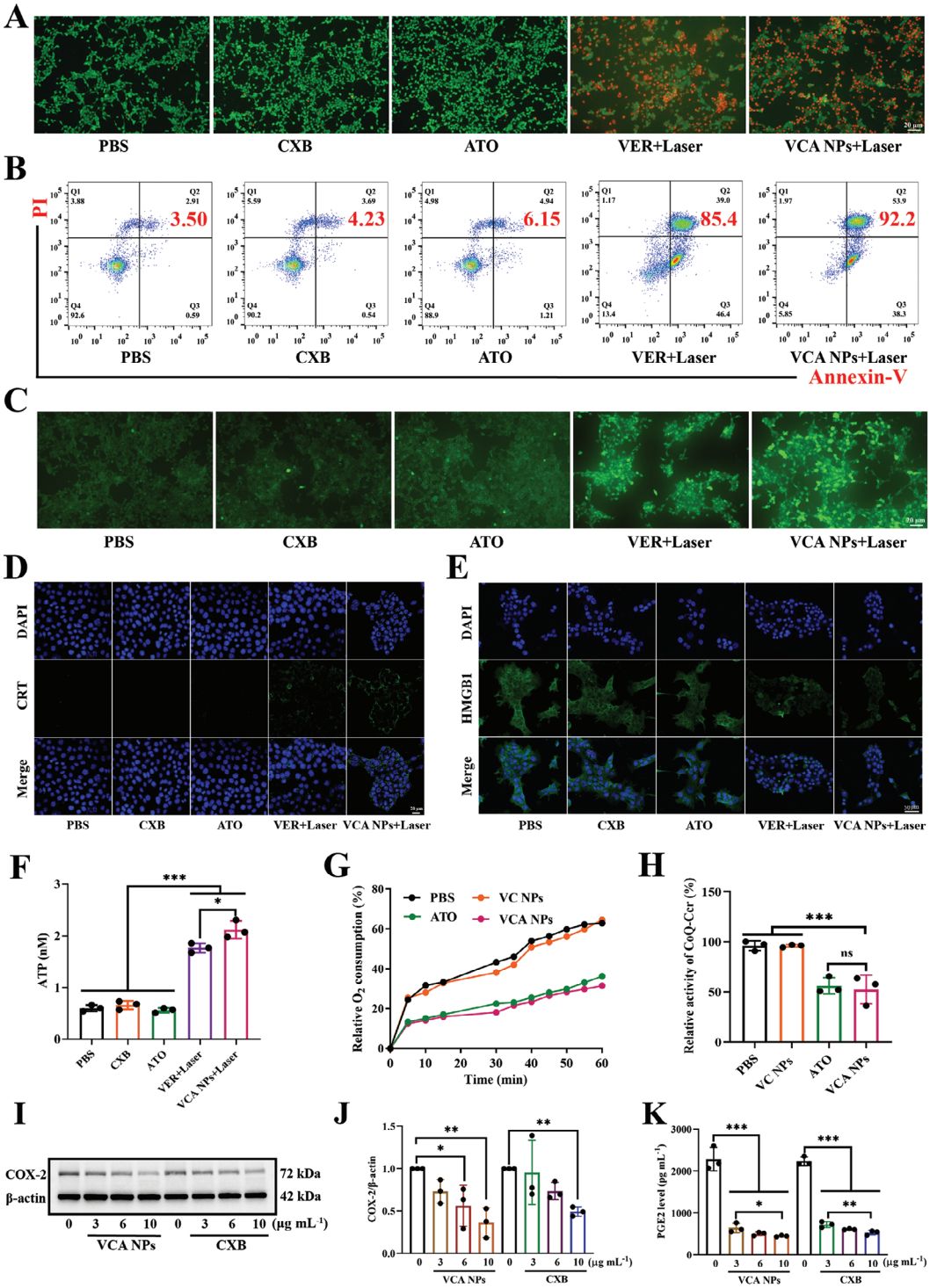

Figure 2. In vitro assessment of pharmacology, immunogenic cell death, and COX-2/PGE2 signaling axis. (A) Live/dead staining of 4T1 cells treated with PBS, CXB, ATO, VER plus laser, and VCA NPs plus laser, scale bar: 20 μm. (B) The apoptosis rate following pharmacologic interventions was detected through flow cytometry. (C) Fluorescent images of intracellular ROS production post-formulation intervention, scale bar: 20 μm. (D) CLSM images of CRT in 4T1 cells post-treatments, scale bar: 20 μm. (E) The fluorescence of HMGB1 in tumor cells was observed via fluorescence microscopy, scale bar: 50 μm. (F) The extracellular ATP content of 4T1 cells after incubation with various formulations, $n = 3$. (G) Relative oxygen consumption of 4T1 cells post-intervention with PBS, VC NPs, ATO, and VCA NPs measured using a dissolved oxygen meter. (H) Relative activity of CoQ-Ccr post-pharmacological intervention, $n = 3$. (I) The expression of COX-2 protein in 4T1 cells after post-treatment with VCA NPs or CXB was detected via Western blot. (J) The grayscale ratio of COX-2/β-actin following intervention with varied concentrations of VCA NPs or CXB, $n = 3$. (K) The extracellular PGE2 levels in 4T1 cells after exposure to CXB or VCA NPs measured using an ELISA kit, $n = 3$. The data are presented as mean ± SD, $^{*}p < 0.05$, $^{**}p < 0.01$, $^{***}p < 0.001$.

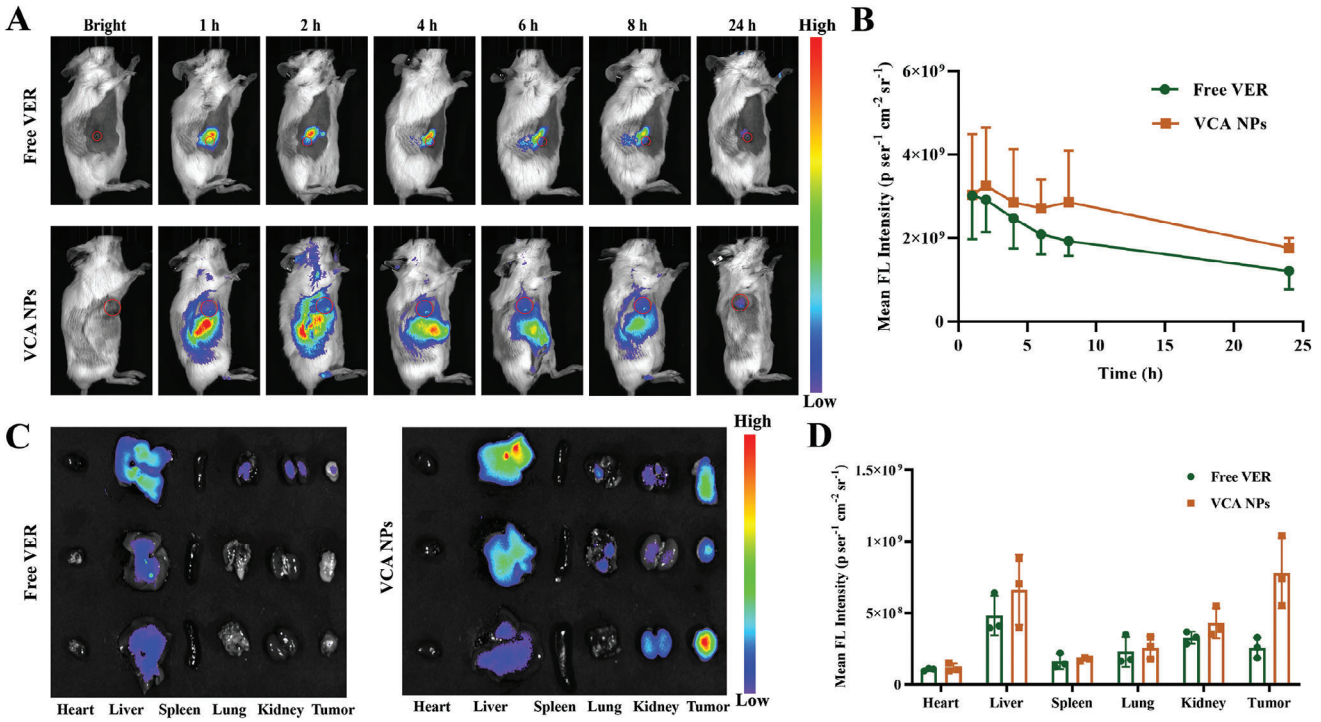

Figure 3. In vivo targeting evaluation. (A) Real-time fluorescence imaging and (B) quantitative images of tumor-bearing mice were obtained following the intravenous injection of either free VER or VCA NPs, $n = 3$. (C) Ex vivo fluorescence images were captured along with (D) the corresponding fluorescence intensity of sacrificed tumors, heart, liver, spleen, lung, and kidney of sacrificed mice 24 h post-injection, $n = 3$.

inclusion of CXB did not impact the rate of oxygen consumption. In recent years, a number of works have demonstrated that ATO is a homolog of the mitochondrial coenzyme Q and can block the electron transfer chain, thereby blocking mitochondrial respiration and decreasing the cellular oxygen consumption rate.[31] To explore the underlying mechanism of this phenomenon, the activity of mitochondrial complex III was assessed using a mitochondrial activity assay kit. The results confirmed that ATO decreased the respiratory oxygen consumption of the tumor cells by inhibiting its function, consequently leading to a reduction of oxygen consumption (Figure 2H). The current experiments validated that ATO decreases cellular oxygen consumption, potentially explaining why VCA NPs can elicit more pronounced immune stimulation, aligning with the documented effects of ATO.

Although PDT assisted by ATO displays promising immunostimulatory effects, a drawback involves excessive inflammation characterized by the upregulation of COX-2 and its downstream signaling molecule PGE2.[32] This inflammatory response diminishes the efficacy of photodynamic immunotherapy.[20,33] Moreover, PGE2 is a common inflammation-associated immunosuppressive factor known to promote tumor immune evasion.[20] Notably, CXB, as a nonsteroidal anti-inflammatory analgesic, can specifically target and diminish COX-2 activity,[10a] which may attenuate this immunosuppression. The impact of various formulation groups containing CXB on COX-2 protein expression was assessed using Western blot analysis. As depicted in Figure S7 (Supporting Information), the expression of COX-2 protein increased significantly upon PDT. Figure 2I,J illustrates that the levels of COX-2 protein were significantly lower in the free CXB and VCA NPs groups compared to the PBS groups, suggesting downregulation of COX-2 protein levels. Correspondingly, the PGE2 levels were substantially decreased in the CXB group compared to the PBS group, reaching the lowest levels in the VCA NPs group (Figure 2K). This suggests a significant inhibition of the COX-2/PGE2 axis. The above findings suggest that CXB could potentially mitigate inflammation-associated immunosuppression, thus benefiting photodynamic immunotherapy.

2.3. In Vivo Biodistribution and Targeting Evaluation

To initially assess the safety of VCA NPs as an intravenous formulation, the hemolysis rate of VCA NPs at various concentrations did not show a significant difference compared to the saline group, and the hemolysis rate of the formulation at high concentrations remained below 5%, indicating favorable biocompatibility of the intravenous formulation (Figure S8, Supporting Information). Moreover, considering the outstanding anti-tumor characteristics of VCA NPs observed in vitro, an in-depth examination of the tumor-targeting capability of these nanoparticles was conducted. Initially, the distribution of VCA NPs within the tumor at various time points was determined using the imaging system. In **Figure 3**A,B, the fluorescence intensity within the tumor area exhibited a rising and then declining trend for VCA NPs, as opposed to free VER. This phenomenon could be linked to the enhanced permeability and retention effect, along with the interaction of specific receptors binding to albumin on the tumor cells. The tumor-targeting capabilities of analogous

albumin-based nanoparticles have also been confirmed in established animal models, including melanoma.[34] In the present study, the peak accumulation of fluorescence intensity was observed at the 2 h, establishing the optimal time for initiating photodynamic therapy for effective treatment in animals. Furthermore, the fluorescence intensity of the isolated major organs and tumor provided additional confirmation that VCA NPs exhibited tumor-targeting characteristics and were primarily metabolized by the liver (Figure 3C,D). These findings collectively validate that the formulated VCA NPs possess significant tumor-targeting capabilities, essential for their synergistic therapeutic efficacy.

2.4. In Vivo Anti-Tumor Study

To assess the in vivo anti-tumor efficacy of VCA NPs, female BALB/c mice were subcutaneously inoculated with 4T1 cells to induce primary and distal tumor formation. The experimental protocol is outlined in **Figure** 4A. No significant differences in body weight were observed among the treatment groups, indicating the excellent in vivo safety profile of each formulation (Figure S9, Supporting Information). The relative primary tumor volume is depicted in Figure 4B. Tumor growth continued rapidly in the saline group, whereas it decelerated in the CXB and ATO groups. Significantly, tumor volume growth decelerated notably in the laser group (VER and VCA NPs), showing statistically significant differences from the saline group. The VCA NPs plus laser group exhibited the most pronounced tumor-suppressing effect, potentially attributable to the amplification of photodynamic immunotherapy. Following the experimental protocol, mice were euthanized at the designated endpoint. Imaging and weighing of treated tumors provided compelling evidence of therapeutic efficacy. The VCA NPs plus laser group exhibited significant tumor growth inhibition, demonstrating a significant difference compared to the saline control group (Figure 4C,D). These results suggest that ATO enhanced VER-mediated photodynamic therapy, while CXB mitigated the inflammation-associated immunosuppressive microenvironment by blocking the COX-2/PGE2 pathway. This synergistic effect ultimately resulted in improved tumor elimination and significant tumor growth inhibition.

To further investigate the potential of this combination therapy to activate the host immune system, a bilateral mouse model was established using BALB/c mice. Following drug treatment, 4T1 cells were subcutaneously injected into the left flank to induce distal tumors. This approach ensured that drug localization was confined to the primary tumor site, enabling the evaluation of the drug's systemic effects on the immune system. As shown in Figure 4E–G, a modest reduction in tumor size was observed in the single-agent group compared to the saline control. In contrast, VCA NPs incorporating ATO, CXB, and VER significantly inhibited the growth of distal tumors, indicating the induction of an immune response by the VCA NPs plus laser. These findings provide additional evidence that the synergistic action of the three agents can significantly reduce the recurrence of distal tumors.

The anti-tumor efficacy of VCA NPs against both primary and distal tumors was demonstrated and further confirmed by histopathological analysis of the tumors. H&E and TUNEL staining revealed partial necrosis in tumors from the CXB, ATO, and VER plus laser groups. In contrast, the VCA NPs plus laser group exhibited significant tumor necrosis characterized by nuclear loss, cytoplasmic damage, and intense green fluorescence (Figure 4H). Ki67 staining indicated a significant suppression of tumor cell proliferation in the VCA NPs plus laser group compared to the other groups (Figure 4H). These pathological findings provide additional support for the potent tumor-suppressing properties of VCA NPs plus laser.

Finally, the weights of individual organs (heart, liver, spleen, lung, and kidney) were measured in all groups, revealing no significant differences (Figure S10, Supporting Information). Histological examination using H&E staining was conducted on each organ, revealing no significant histopathological damage in any treatment group (Figure S11, Supporting Information). In conclusion, the results of the safety evaluation confirms that the excellent safety profile of the nanomedicine and its potential for clinical application.

2.5. Systemic Anti-Tumor Immune Response In Vivo

Systemic therapy exhibited outstanding efficacy in both ex vivo and in vivo settings. Further investigation is warranted to explore its potential correlation with inducing phenotypic alterations in immune cells, subsequently activating systemic immunity. DC maturation in lymph nodes is a critical step in initiating host immunity.[35] Studies have shown that PDT promotes DC uptake of tumor-associated antigens, contributing to DC maturation.[36] First, double-positive cells ($CD80^+CD86^+$) from the inguinal lymph nodes of the primary tumor on day nine were sorted by flow cytometry. These cells originated from the $FVS780^-CD45^+MHC\text{-}II^+CD11c^+$ cell population, as shown in **Figure** 5A. The mature DC ratio increased by 1.6-, 1.7-, 2.5-, and 3.8-fold in the CXB, ATO, VER plus laser, and VCA NPs plus laser groups, respectively, compared to the saline group (Figure 5B). This suggests that VCA NPs plus laser enhance DC maturation, effectively triggering immune responses, attributed to increased tumor immunogenicity and blockade of the COX-2/PGE2 axis, thereby boosting photodynamic immunotherapy.

Overall, the intensity of host immune system activation is contingent on the stimulation of cytotoxic T lymphocytes ($CD8^+$ T cells), acting as a positive feedback factor, and the suppression of regulatory T cells (Tregs), acting as a negative feedback factor.[37] Subsequently, $CD8^+$ T lymphocytes derived from $CD3^+$ T cells and $FOXP3^+$ lymphocytes derived from $CD4^+$ T cells were sorted by flow cytometry (Figure S12, Supporting Information). A significant increase in tumor infiltration of $CD8^+$ T lymphocytes was observed in the VCA NPs plus laser group, as shown in Figure 5C, surpassing the saline group by ≈2-fold. This data demonstrates that the integrated approach yielded a substantial impact on promoting $CD8^+$ T lymphocyte infiltration, a key factor in inhibiting tumor growth. Conversely, a significant decrease of ≈2.6-fold in FOXP3 levels was observed within the VCA NPs plus laser group compared to the saline group, as shown in Figure 5D. This reduction suggests a significant suppression of immunosuppressive factors in the tumor microenvironment. The decrease in FOXP3 expression may be linked to the improvement of the tumor's hypoxic microenvironment by ATO, consistent with previous findings.[38] Taken together, these findings

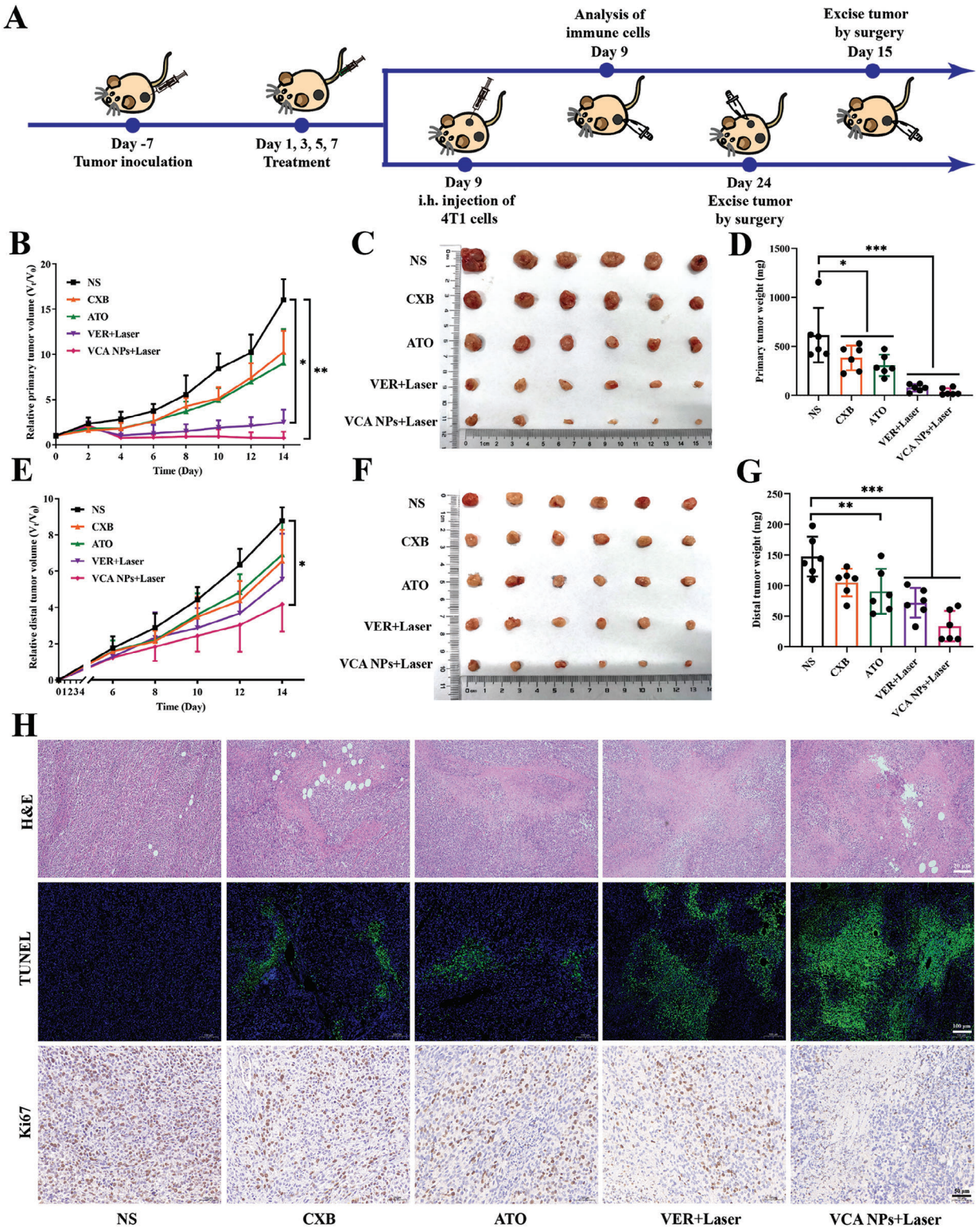

Figure 4. In vivo synergistic inhibition of primary tumor and distal tumor. (A) Schematic depiction of primary and distal tumors in 4T1 tumor-bearing mice following treatment with various formulations. (B) Changes in relative growth curves of the primary tumor under different treatments, including NS, CXB, ATO, VER plus laser, and VCA NPs plus laser (at a light intensity of 200 mW cm^{-2} for 10 min), $n = 6$. (C) The photograph and (D) average weight of isolated tumors obtained from different groups, $n = 6$. (E) The alterations in the relative volume of distal tumor in mice post-treatment with diverse formulations, $n = 6$. (F) The images of isolated distal tumors and (G) average tumor weights in mice treated receiving different formulations, $n = 6$. (H) H&E, TUNEL, and Ki67 staining of primary tumors treated with various regimens, scale bar: 20, 100, and 50 µm. The data are presented as mean ± SD, $*p < 0.05$, $**p < 0.01$, $***p < 0.001$.

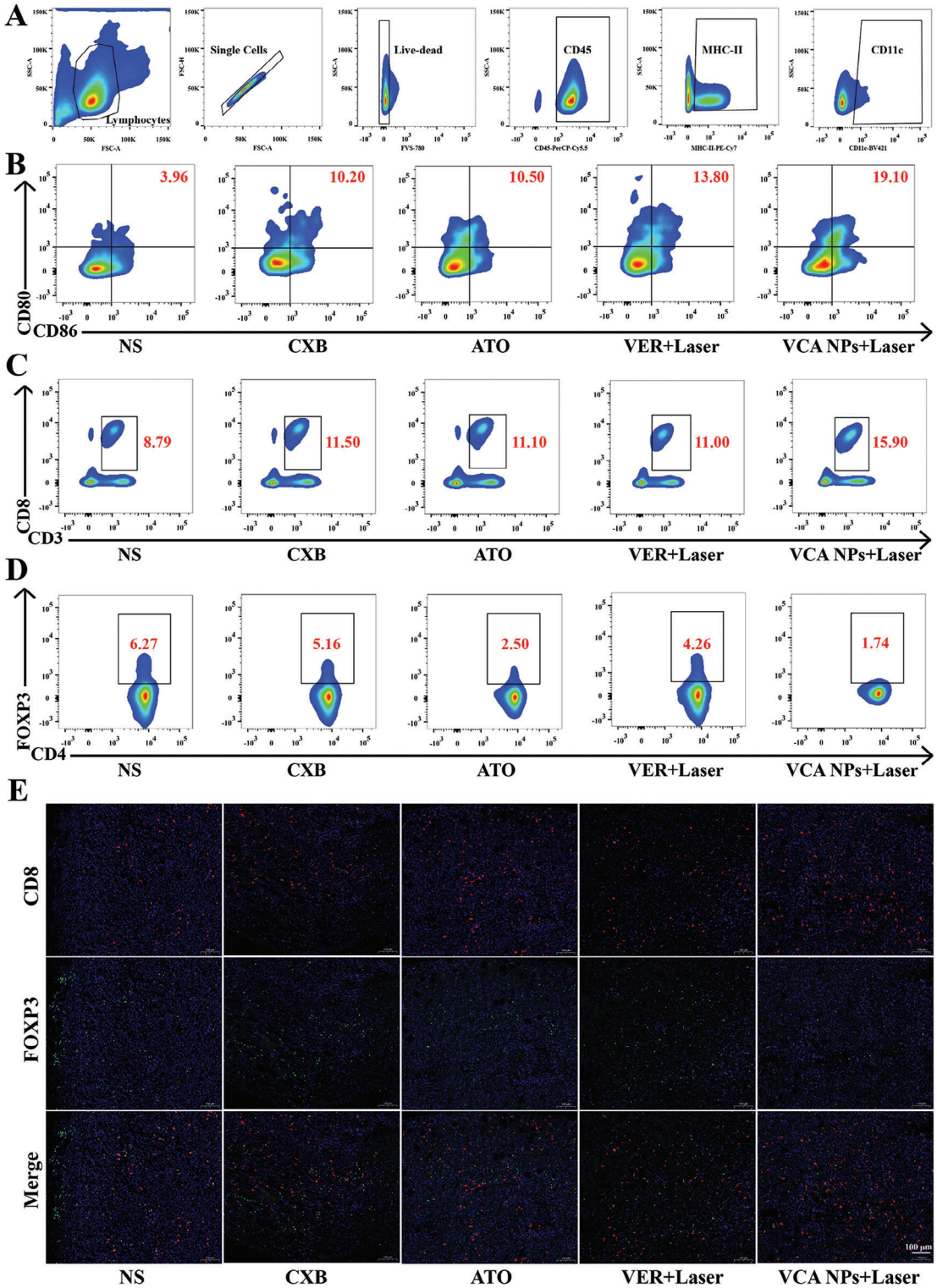

Figure 5. In vivo examination of anti-tumor immune responses. (A) The gating strategy ($FVS780^{-}CD45^{+}MHC\text{-}II^{+}CD11c^{+}$) for identifying mature dendritic cell clusters using flow cytometry. (B) The $CD80^{+}CD86^{+}$ double-positive cell population is listed in (A). (C) Flow cytometry plots of $CD3^{+}CD8^{+}$ and (D) $CD4^{+}FOXP3^{+}$ in primary tumor sections from mice. (E) Immunofluorescence images of $CD8^{+}$ (red), $FOXP3^{+}$ (green), and DAPI (blue) in distal tumor sections from mice, scale bar: 100 μm.

indicate that VCA NPs plus laser can induce potent local immune responses within the tumor microenvironment.

Moreover, T lymphocytes derived from the distal tumor site were examined to demonstrate the systemic immune response triggered by the VCA NPs plus laser. Briefly, immunofluorescence staining was used to label $CD8^+$ (red) and $FOXP3^+$ (green) cells. As shown in Figure 5E, red fluorescence intensity was elevated in the groups receiving individual treatment (CXB, ATO, and VER plus laser) compared the saline group. Notably, the highest red fluorescence intensity in tumor sections was observed in the VCA NPs plus laser group, suggesting a pronounced systemic immune response. Conversely, the green fluorescence signal decreased in the groups treated solely with CXB, ATO, and VER plus laser, with VCA NPs plus laser displaying the lowest green fluorescence intensity within the tumor area, suggesting amelioration of the tumor's immunosuppressive milieu. These results collectively confirm a substantial activation of the host immune system.

2.6. In Vivo Evaluation of Anti-Tumor Recurrence and Anti-Metastatic Effect

Furthermore, the anti-tumor immune response elicited by the integrated approach was validated in models simulating tumor recurrence and lung metastasis. The protocols illustrating the anti-tumor recurrence and anti-metastatic effects are shown schematically in **Figure 6A**. As shown in Figure 6B, tumors in the saline, CXB, and ATO groups recurred at the original site within 2 weeks. In contrast, only 4 mice in the laser-treated groups (VER and VCA NPs) showed signs of recurrence. The tumors were further weighed, and while some mice in the VCA NPs plus laser group did experience recurrence in the primary site, their tumor sizes were all significantly smaller compared to those in the saline group (Figure 6C). Tumor recurrence experiments unequivocally validated the effectiveness of VCA NPs plus laser in suppressing tumor regrowth. Additionally, they provided compelling evidence that the utilization of triple-agent combinations could elicit a robust systemic immune response. Subsequently, as illustrated in Figure 6D, the group administered with saline exhibited the most pronounced lung tumor metastasis, resulting in one fatality within the observation period. The count of lung tumor metastatic nodules markedly decreased in subjects receiving drug therapy, with the lowest nodular presence noted in the VCA NPs plus laser group. Consistently, H&E staining results of the lung tissue aligned with those depicted in Figure 6D. While the saline group exhibited numerous tumor foci, notably fewer foci were observed in the lungs of the CXB, ATO, and VER plus laser groups, with the least number of foci identified in the VCA NPs plus laser group (Figure 6E). The results suggest that the VCA NPs plus laser group displayed minimal cancerous lesions. The capacity of VCA NPs plus laser to hamper lung metastasis was linked to the activation of the immune system, affirming the effectiveness of VCA NPs plus laser as a top-tier nanomedicine for impeding tumor metastasis.

Finally, effector memory T cells (Tem) were identified via flow cytometry, showcasing their ability to promptly mount responses upon encountering external stimuli.[39] Following the intravenous administration of 4T1 cells, the spleens of each group of mice were harvested and the proportion of Tem cells ($CD62L^-CD44^+$) was selected from the designated gate ($FVS780^-CD45^+CD3^+CD8^+$) (Figure S13, Supporting Information). The VCA NPs plus laser group exhibited an ≈2-fold increase in Tem cell proportion compared to the saline group, confirming the ability to elicit a rapid immune response upon re-exposure to external stimuli, such as 4T1 cells (Figure 6F,G). Therefore, our VCA NPs plus laser exhibit strong immune memory properties that could confer long-term immune reactivity to suppress tumor progression.

3. Conclusion

This study aimed to amplify PDT by developing a self-delivery nanomedicine to stimulate a systemic immune response against tumor recurrence and metastasis. The co-loading of CXB, ATO, and VER, supplemented by HSA as a carrier, led to the formation of stable, uniformly spherical nanomedicine. The nanomedicine demonstrated promising efficacy in inhibiting the proliferation of 4T1 cells and inducing apoptosis in vitro while also exhibiting excellent tumor-targeting properties in vivo. In addition, the assistance of ATO amplified PDT-initiated immunogenic cell death to regulate the hypoxic microenvironment. Moreover, CXB enhanced the cascade of immune activation by blocking the COX-2/PGE2 axis, thus alleviating the hyperinflammatory and immunosuppressive tumor microenvironment induced by PDT. Ultimately, our approach effectively triggered the maturation of DCs, infiltration of $CD8^+$ T cells, while concurrently suppressing FOXP3 expression into the tumor. Taken together, our nanomedicine notably suppressed primary tumors, distal tumors, post-operative recurrence, and lung metastasis, indicating promising prospects for tailored and personalized nanomedicine therapy across various solid tumors, including triple-negative breast cancer.

4. Experimental Section

Materials: Verteporfin (HY-B0146) was obtained from MedChemExpress (MCE). Celecoxib (C129279) was supplied by Aladdin Industrial Corporation. Atovaquone (PHR1591) was purchased from Sigma–Aldrich. Human serum albumin (S12018) was supplied by Yuanye Bio-Technology Co., Ltd. FBS was provided by PAN-Biotech GmbH. Methylthiazolyldiphenyl-tetrazolium bromide (MTT, ST316), COX2/cyclooxygenase two rabbit monoclonal antibody (AF1924), and β-actin rabbit monoclonal antibody (AF5003) were supplied by Beyotime Biotechnology Co., Ltd. The PGE2 ELISA kit (EK8103) was supplied by MultiSciences Biotech Co., Ltd. HRP-labeled goat anti-rabbit monoclonal antibody (KGAA35), RPMI-1640 medium, and 4′,6-diamidino-2-phenylindole (DAPI, KGR0001) were purchased from KeyGEN BioTECH Corp., Ltd. The rabbit anti-CRT/BF488 (bs-5913R) or anti-HMGB1/FITC (bs-20633R) were obtained from Bioss Co., Ltd. Flow-through antibodies, such as PerCP-Cy5.5-labeled CD45 (561869), FITC-labeled CD3 (561827), PE-Cy7-labeled CD8 (100721), APC-labeled CD4 (561091), PE-labeled FOXP3 (563101), BV421-labeled CD11c (565451), PE-labeled CD80 (561955), APC-labeled CD86 (561964), FITC-labeled CD8 (561966), PE-labeled CD3 (561799), PE-Cy7-labeled CD44 (560569), and FVS-780 (565388) were obtained from BD Biosciences (USA). PE-Cy7-labeled MHC-II (107629) and BV421-labeled CD62L (104435) were supplied by BioLegend (USA).

Cells: 4T1 cells were cultured in RPMI-1640 medium supplemented with 10% FBS and 1% penicillin-streptomycin solution in a humidified incubator at 37 °C with 5% CO_2.

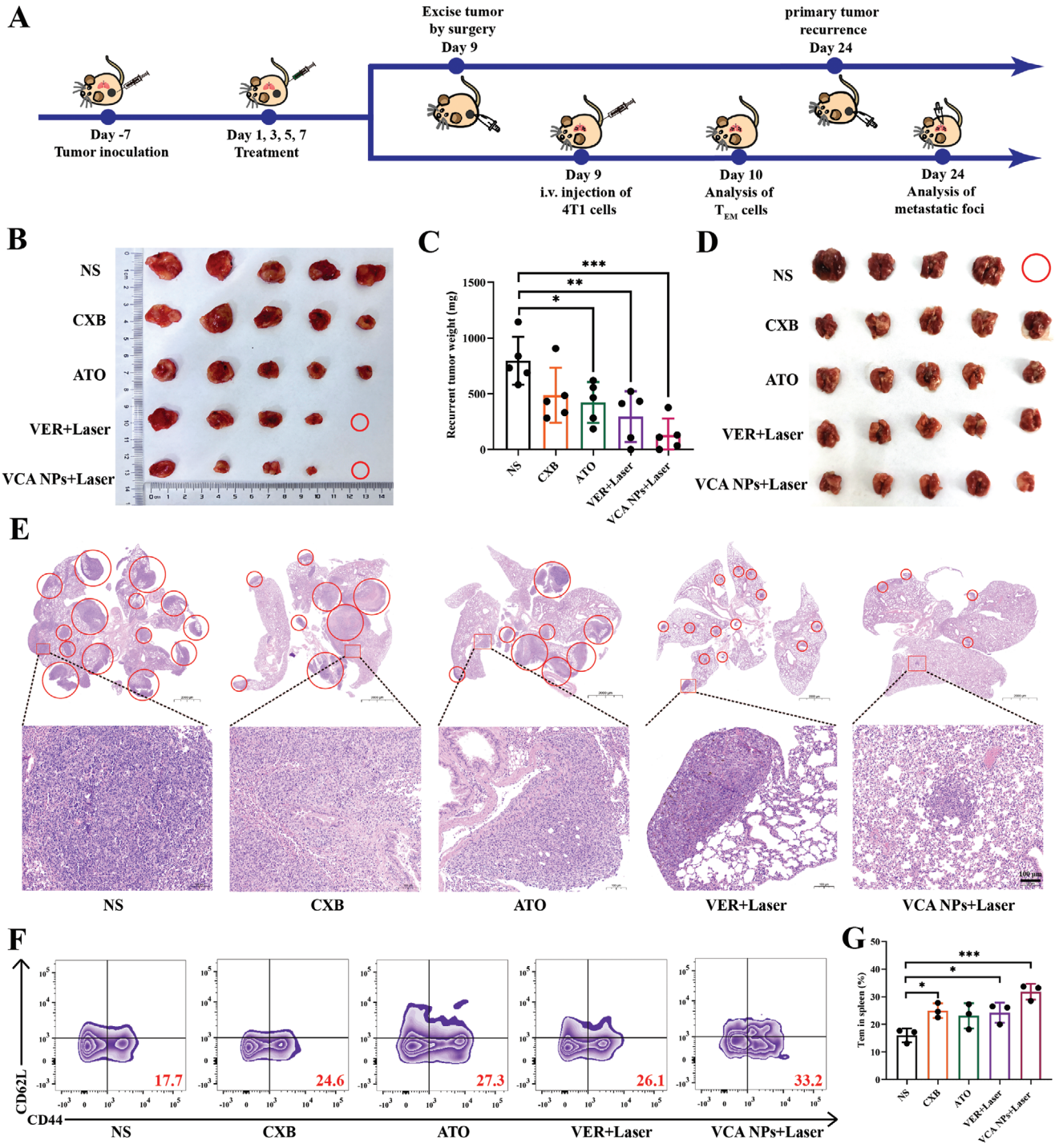

Figure 6. The in vivo synergistic inhibition of tumor recurrence and metastasis in 4T1 tumor-bearing mice. (A) The scheme of post-operative recurrence and metastasis following various treatments. (B) The ex vivo post-operative images and (C) the weight of recurrent tumors in the primary site, $n = 5$. (D) Images of isolated lung tissue from the metastatic tumor model, $n = 5$. (E) Representative H&E staining of lung tissue at different magnifications, scale bar: 2000 and 100 µm. (F) Flow cytometry plots and (G) quantitative analysis of effector memory T cells (Tem) in the spleens, $n = 3$. The data are presented as mean ± SD, $^{*}p < 0.05$, $^{***}p < 0.001$.

Animals: Female BALB/c mice (6–8 weeks old) were sourced from the Laboratory Animal Center of 900th Hospital of the Joint Logistics Team. All animal experiments were supervised and approved by the Institutional Animal Care and Use Committee of 900th Hospital of the Joint Logistics Team (approval number: 2023-37).

Synthesis of VCA NPs: VER, CXB, and ATO nanoparticles (VCA NPs) were synthesized via a co-assembly method using HSA as a carrier. Specifically, 300 μg of VER, 600 μg of CXB, and 300 μg of ATO were dissolved in 200 μL of N, N-Dimethylformamide (DMF) and then added dropwise to an aqueous solution containing 10 mg of HSA under sonication. To ensure complete co-assembly, the drug-containing solution was sonicated for 20 min under light protection, followed by purification of the VCA NPs through dialysis.

Characterizations of VCA NPs: The particle size and zeta potential of VCA NPs were measured using a dynamic light scattering instrument (DLS, Malvern). The UV–vis absorption spectra of VER, CXB, ATO, HSA, and VCA NPs were analyzed using a UV–vis spectrophotometer (TU-1901). The morphology of the VCA NPs was examined through TEM. Various drug solutions were visually examined, and the presence of VCA NPs were confirmed through the Tyndall effect. The VCA NPs was immersed in water, PBS, saline, and 1640 medium with 10% FBS for seven days. The particle size and PDI were assessed using DLS to evaluate the stability of the VCA NPs. To determine the drug's encapsulated efficiency (EE) and loaded efficiency (LC), high-performance liquid chromatography (HPLC, SHIMADZU, LC-20A) was employed to analyze the content of the VCA NPs. The detection wavelengths were 427 nm for VER, 245 nm for CXB, and 276 nm for ATO, respectively. The EE and LC of VCA NPs were calculated using the following formulas: EE (%) = purified drug content/quantity of drug input, LC (%) = purified drug content/quantity of total drug and carrier input.

Lyophilized Powder of VCA NPs: Lyophilized formulations of VCA NPs were prepared by incorporating lyophilization protectants (1% mannitol and 1% sucrose), and the alterations in particle size or morphology were evaluated post-lyophilization.

Cellular Uptake: Using the fluorescence absorption properties of VER, this study examined the fluorescence distribution intensity of VCA NPs within tumor cells at the first, second, and fourth hours post-administration. Flow cytometry was employed to analyze the cellular uptake kinetics of VCA NPs. 4T1 cells were seeded at a density of 3×10^5 cells per well in six-well plates and incubated overnight. Then the culture medium was replaced with VCA NPs (VER concentration: 10 μg mL^{-1}) and incubated for varying durations. Subsequently, the cells were suspended in PBS and quantified using flow cytometry.

Cytotoxicity Assay: The cytotoxicity of various concentrations of VER, CXB, ATO, and VCA NPs was assessed using the MTT assay (VER concentration range: 0.3–20 μg mL^{-1}). 4T1 cells were seeded in 96-well plates at a density of 5000 cells per well and incubated overnight. Subsequently, the cells were treated with fresh medium containing various formulations. After 24 h of incubation, 20 μL of MTT solution (5 mg mL^{-1}) was dispensed into each well and incubated for another 2 h. Subsequently, the medium was aspirated, and dimethyl sulfoxide (DMSO) was added and thoroughly mixed by shaking. The absorbance value was then measured at 570 nm.

In Vitro Photodynamic Therapy: 4T1 cells were plated in 96-well plates at a density of 5000 cells per well and cultured for 4 h with both free VER and VCA NPs across a concentration range of 0.125–2 μg mL^{-1}. Subsequently, the cells were exposed to a 635 nm laser (0.5 mW cm^{-2}, 10 min) and then further incubated in a controlled environment for an additional 20 h. Photodynamic therapy efficacy was assessed by employing MTT reagents following the previously outlined procedure.

Calcein-AM/PI Staining Evaluation: The therapeutic effectiveness of VCA NPs was further evidenced through the identification of living and deceased cells using Calcein-AM/PI kits (KeyGEN, KGAF001). Specifically, 4T1 cells were incubated with PBS, CXB, ATO, and the laser group (VER and VCA NPs) with a 635 nm laser (0.5 mW cm^{-2}, 10 min), with a VER concentration of 0.5 μg mL^{-1}. The cells were stained following the protocol of the kit and captured through fluorescence microscopy.

Evaluation of Cell Apoptosis: Quantification of VCA NPs-induced apoptosis in 4T1 cells was conducted. In summary, 4T1 cells were seeded in six-well plates and treated with PBS, CXB, ATO, VER plus laser, and VCA NPs plus laser (0.5 mW cm^{-2}, 10 min). The concentration of VER used was 0.5 μg mL^{-1}. Subsequently, the cells were stained with Annexin V-APC/Cyanine7/PI (Elabscience, E-CK-A229) following the kit protocol and then analyzed using flow cytometry.

Detection of ROS: The generation of cellular ROS was assessed using DCFH-DA (Merck Millipore, 287810). Specifically, 4T1 cells were treated with PBS, CXB, ATO, and the laser group (consisting of VER and VCA NPs). A 635 nm laser was applied for 10 min at a power density of 0.5 mW cm^{-2}. The administered dose of VER was 0.5 μg mL^{-1}. The DCFH-DA reagent was introduced following the manufacturer's guidelines, and this was followed by laser treatment. The resulting green fluorescence was visualized using fluorescence microscopy.

Evaluation of ICD: 4T1 cells were exposed to various treatments, including PBS, CXB, ATO, VER plus laser, and VCA NPs plus laser. Following drug administration (VER concentration: 0.5 μg mL^{-1}, laser power: 0.5 mW cm^{-2}, duration: 10 min), to assess CRT exposure and HMGB1 distribution, the cells were sealed with 3% BSA, and then subjected to overnight incubation with anti-CRT/BF488 or anti-HMGB1/FITC at 4 °C. To facilitate HMGB1 staining, a membrane disruptor was employed. Subsequently, the cell nuclei were stained using DAPI and visualized through CLSM, fluorescence microscopy, or flow cytometry. ATP secretion was assessed by analyzing the cell supernatants with an ATP assay kit (S0027, Beyotime).

Evaluation of Hypoxia In Vitro: 4T1 cells were cultured in a 60 × 15 mm cell culture dish at a density of 2×10^6 cells per well and incubated for 24 h with PBS, free ATO, VC NPs, and VCA NPs at a concentration of 10 μg mL^{-1} ATO. On the one hand, a dissolved oxygen meter probe was immersed in the medium and sealed with a liquid paraffin solution to monitor dissolved oxygen changes over a 1-h period. On the other hand, the activity of mitochondrial complex III was assessed using the CoQ-cytochrome C reductase activity assay kit (CoQ-Ccr, Solarbio, BC3240). Absorbance readings at 550 nm were measured utilizing a spectrophotometer (TECAN Infinite E Plex).

Evaluation of COX-2 Protein and PGE2: The expression of COX-2 protein in 4T1 cells following treatment with CXB and VCA NPs was assessed through Western blot analysis. In the experimental setup, 4T1 cells were seeded in 25 mm^2 culture dishes and treated with free CXB and VCA NPs at varying concentrations (CXB: 3, 6, 10 μg mL^{-1}) for 24 h. Whole protein lysates were collected and subjected to electrophoresis, followed by membrane transfer and blocking with 5% skim milk powder. Primary antibodies (COX-2 or β-actin, 1:2000 dilution, rabbit anti-mouse) were incubated overnight, and secondary antibodies (1:5000 dilution, goat anti-rabbit) were incubated at room temperature for 1 h. The samples were then visualized using an exposure apparatus. The identical dosing regimen was employed to assess the expression of PGE2 in cellular supernatants using a PGE2 ELISA kit. Each experiment was conducted in triplicate.

Hemolysis Test: 2% (*v*/*v*) suspension of erythrocytes was prepared, using saline as a negative control and purified water as a positive control. Erythrocyte solutions containing various concentrations of VCA NPs (2.5–50 μg mL^{-1}) were incubated at 37 °C for 4 h. After centrifugation, the supernatant was collected and assayed at an OD of 540 nm to determine the hemolysis rate.

In Vivo Biodistribution: Once the tumor volume of the mice reached ≈100 mm^3, free VER and VCA NPs were intravenously administered. The accumulation of fluorescence in the tumor area at various time points was monitored using a small-animal live-imaging instrument (AniView, BLT). After 24 h, the main organs and tumor tissues of the mice were dissected. Fluorescence imaging of the isolated organs and tumor was conducted using an imaging instrument and subjected to quantitative fluorescence analysis at the ex vivo level.

In Vivo Anti-Primary Tumor: Female BALB/c mice (6–8 weeks old) were subcutaneously injected with 4T1 cells (1×10^6 cells) in the right axilla to establish a primary tumor model. Once the tumors reached a size of 50–100 mm^3, the mice were randomly divided into five groups: NS (saline), CXB, ATO, VER plus laser, and VCA NPs plus laser. The formulations were administered every two days, with doses of VER at 3 mg kg^{-1}, CXB at 5.2 mg kg^{-1}, and ATO at 3 mg kg^{-1}. Two hours after administration, the

laser groups were irradiated with a 635 nm laser for 10 min at a power density of 200 mW cm^{-2}. Tumor size was recorded every other day using the formula: $V = L \times W^2/2$, where L and W represent the length and width of the tumor, respectively. Upon completion of the treatment, the mice were euthanized by cervical dislocation. Lymph nodes and tumors were collected for the phenotypic analysis of immune cells. On day 15, the remaining mice were euthanized, and both tumors and major organs were dissected for analysis using H&E staining to evaluate apoptosis and biosafety. Tumors were further assessed at the pathological level by staining with TUNEL and Ki67 immunohistochemistry to investigate the impact of VCA NPs plus laser on tumor inhibition.

In Vivo Immune Response Analysis: On the ninth day, fresh inguinal lymph nodes and tumors were harvested using surgical scissors. The tissues were then homogenized into a single-cell suspension using a tissue grinder, ensuring a gentle grinding technique to minimize cellular debris. Mature dendritic cells ($CD80^+CD86^+$) were quantified using flow cytometry by gating for $FVS780^-CD45^+MHC\text{-}II^+CD11c^+$. Cytotoxic T cells ($CD8^+$, gating from $FVS780^-CD45^+CD3^+$) and regulatory T cells ($FOXP3^+$, gating from $FVS780^-CD45^+CD3^+CD4^+$) within primary tumors were identified utilizing flow cytometry.

In Vivo Anti-Distal Tumor: A bilateral tumor model was employed to assess the therapeutic efficacy of VCA NPs plus laser. In essence, a distal tumor model was created by inoculating 4T1 cells (5×10^5 cells) into the left axilla on the second day following the completion of four treatment cycles targeting the primary tumor. Subsequently, tumor volume was monitored every two days up to day 24. Following this, the mice were euthanized, tumors were weighed, and distal tumor volume curves were graphed. Additionally, the distal tumor sections were stained for $CD8^+$ (red), $FOXP3^+$ (green), and DAPI (blue).

Evaluation of Primary Tumor Recurrence: Following pharmacological intervention as per the primary tumor model, the primary tumor was excised surgically. Within 2 weeks, tumor recurrence was observed at the primary site. The post-operative tumors were photographed and weighed to assess the degree of immune system activation.

In Vivo Anti-Metastasis Experiments: Following pharmacological intervention on the primary tumors, 4T1 cells resuspended in saline (2×10^5 cells) were intravenously injected to establish a lung metastatic tumor model. Subsequently, three mice from each group were euthanized the next day, and their spleens were dissected. Single-cell suspensions from the spleens were obtained by homogenization. Effector memory T cells ($CD44^+CD62L^-$, gated from $FVS780^-CD45^+CD3^+CD8^+$) were quantified using flow cytometry to evaluate the organism's immune responsiveness upon re-exposure to external stimuli. The remaining mice were monitored for an additional two weeks. Then, the lung tissue was removed and photographed. H&E staining was used to examine the metastatic nodules in the lung tissue.

Statistical Analysis: Data were expressed as mean ± SD. Student's *t*-test or one-way analysis of variance followed by Tukey's multiple comparisons test was used to compare between two groups or multiple groups, respectively. Significant levels were denoted as $*p < 0.05$, $**p < 0.01$, and $***p < 0.001$.

Supporting Information

Supporting Information is available from the Wiley Online Library or from the author.

Acknowledgements

X.Q.F., Y.Z., and W.J.L. contributed equally to this work. This research was supported by the Natural Science Foundation of Fujian Province (Grant no. 2024J08094) and the Fujian Medical University Startup Fund for Scientific Research (Grant no. 2023QH1353). The authors gratefully the Public Technology Service Center (Fujian Medical University, Fuzhou, China) for technical assistance.

Conflict of Interest

The authors declare no conflict of interest.

Data Availability Statement

The data that support the findings of this study are available from the corresponding author upon reasonable request.

Keywords

cascade immune activation, COX-2/PGE2, hypoxia, photodynamic immunotherapy, triple-negative breast cancer

Received: October 30, 2024
Revised: December 29, 2024
Published online:

[1] R. A. Leon-Ferre, M. P. Goetz, *BMJ* **2023**, *381*, e071674.
[2] R. Everatt, D. Gudavičienė, *BMC Public Health* **2022**, *22*, 1812.
[3] a) T. E. Keenan, S. M. Tolaney, *JNCCN* **2020**, *18*, 479; b) Y. Liu, Y. Hu, J. Xue, J. Li, J. Yi, J. Bu, Z. Zhang, P. Qiu, X. Gu, *Mol. Cancer* **2023**, *22*, 145.
[4] V. Geurts, M. Kok, *Curr. Treat. Options Oncol.* **2023**, *24*, 628.
[5] a) Q. Yin, L. Wu, L. Han, X. Zheng, R. Tong, L. Li, L. Bai, Y. Bian, *Front. Immunol.* **2023**, *14*, 1167975; b) M. Yi, X. Zheng, M. Niu, S. Zhu, H. Ge, K. Wu, *Mol. Cancer* **2022**, *21*, 28.
[6] D. Hanahan, R. A. Weinberg, *Cell* **2011**, *144*, 646.
[7] K. Luo, L. Yang, C. Yan, Y. Zhao, Q. Li, X. Liu, L. Xie, Q. Sun, X. Li, *Small* **2023**, *19*, 2302834.
[8] C. Huang, B. Lin, C. Chen, H. Wang, X. Lin, J. Liu, Q. Ren, J. Tao, P. Zhao, Y. Xu, *Adv. Mater.* **2022**, *34*, 2207593.
[9] Q. Wu, Z. Li, X. Zhou, Z. Wei, S. Ramadan, Y. Xu, L. Xu, D. Li, *Small* **2024**, *20*, 2306766.
[10] a) S. Zelenay, A. G. van der Veen, J. P. Böttcher, K. J. Snelgrove, N. Rogers, S. E. Acton, P. Chakravarty, M. R. Girotti, R. Marais, S. A. Quezada, E. Sahai, C. Reis e Sousa, *Cell* **2015**, *162*, 1257; b) A. Santiso, A. Heinemann, J. Kargl, *Pharmacol. Rev.* **2024**, *76*, 388.
[11] a) S. B. Lacher, J. Dörr, G. P. de Almeida, J. Hönninger, F. Bayerl, A. Hirschberger, A.-M. Pedde, P. Meiser, L. Ramsauer, T. J. Rudolph, N. Spranger, M. Morotti, A. J. Grimm, S. Jarosch, A. Oner, L. Gregor, S. Lesch, S. Michaelides, L. Fertig, D. Briukhovetska, L. Majed, S. Stock, D. H. Busch, V. R. Buchholz, P. A. Knolle, D. Zehn, D. Dangaj Laniti, S. Kobold, J. P. Böttcher, *Nature* **2024**, *629*, 417; b) M. Morotti, A. J. Grimm, H. C. Hope, M. Arnaud, M. Desbuisson, N. Rayroux, D. Barras, M. Masid, B. Murgues, B. S. Chap, M. Ongaro, I. A. Rota, C. Ronet, A. Minasyan, J. Chiffelle, S. B. Lacher, S. Bobisse, C. Murgues, E. Ghisoni, K. Ouchen, R. Bou Mjahed, F. Benedetti, N. Abdellaoui, R. Turrini, P. O. Gannon, K. Zaman, P. Mathevet, L. Lelievre, I. Crespo, M. Conrad, et al., *Nature* **2024**, *629*, 426.
[12] Z. Liu, Z. Xie, W. Li, X. Wu, X. Jiang, G. Li, L. Cao, D. Zhang, Q. Wang, P. Xue, H. Zhang, *J. Nanobiotechnol.* **2021**, *19*, 160.
[13] W. Li, J. Yang, L. Luo, M. Jiang, B. Qin, H. Yin, C. Zhu, X. Yuan, J. Zhang, Z. Luo, Y. Du, Q. Li, Y. Lou, Y. Qiu, J. You, *Nat. Commun.* **2019**, *10*, 3349.
[14] F. Yang, S. Li, Q. Ji, H. Zhang, M. Zhou, Y. Wang, S. Zhang, J. Sun, Z. He, C. Luo, *Adv. Sci. (Weinh)* **2024**, *11*, 2405583.
[15] K. Tang, L. Zhu, J. Chen, D. Wang, L. Zeng, C. Chen, L. Tang, L. Zhou, K. Wei, Y. Zhou, J. Lv, Y. Liu, H. Zhang, J. Ma, B. Huang, *Cancer Res.* **2021**, *81*, 4949.

[16] a) B. Harris, S. Saleem, N. Cook, E. Searle, *J. Exp. Clin. Cancer Res.* **2022**, *41*, 318; b) Y. Wan, L.-H. Fu, C. Li, J. Lin, P. Huang, *Adv. Mater.* **2021**, *33*, 2103978.
[17] I. Vercellino, L. A. Sazanov, *Nat. Rev. Mol. Cell Biol.* **2022**, *23*, 141.
[18] L.-P. Zhao, R.-R. Zheng, H.-Q. Chen, L.-S. Liu, X.-Y. Zhao, H.-H. Liu, X.-Z. Qiu, X.-Y. Yu, H. Cheng, S.-Y. Li, *Nano Lett.* **2020**, *20*, 2062.
[19] a) J.-M. Lai, P.-L. Chen, Q.-Y. Shi, Y.-Q. Xie, G. Jiaerheng, L.-H. Liu, *Adv. Healthcare Mater.* **2024**, *13*, 2400367; b) Y. Liu, J. He, M. Li, K. Ren, Z. Zhao, *ACS Appl. Mater. Interfaces* **2024**, *16*, 6879.
[20] R.-J. Kong, Y.-M. Li, J.-Q. Huang, N. Yan, Y.-Y. Wu, H. Cheng, *ACS Appl. Mater. Interfaces* **2023**, *15*, 59165.
[21] C. He, Z. Tang, H. Tian, X. Chen, *Adv. Drug Delivery Rev.* **2016**, *98*, 64.
[22] M. Majidinia, M. Mirza-Aghazadeh-Attari, M. Rahimi, A. Mihanfar, A. Karimian, A. Safa, B. Yousefi, *IUBMB Life* **2020**, *72*, 855.
[23] a) M. Yokoyama, *J. Drug Target.* **2014**, *22*, 576; b) P. Thakor, V. Bhavana, R. Sharma, S. Srivastava, S. B. Singh, N. K. Mehra, *Drug Discovery Today* **2020**, *25*, 1718.
[24] X. Lang, X. Wang, M. Han, Y. Guo, *Int. J. Nanomed.* **2024**, *19*, 4533.
[25] a) T. Safra, F. Muggia, S. Jeffers, D. D. Tsao-Wei, S. Groshen, O. Lyass, R. Henderson, G. Berry, A. Gabizon, *Ann. Oncol.* **2000**, *11*, 1029; b) E. Blanco, H. Shen, M. Ferrari, *Nat. Biotechnol.* **2015**, *33*, 941.
[26] a) F. F. Visentini, A. A. Perez, L. G. Santiago, *Crit. Rev. Food Sci. Nutr.* **2023**, *63*, 7238; b) Z. Shi, M. Luo, Q. Huang, C. Ding, W. Wang, Y. Wu, J. Luo, C. Lin, T. Chen, X. Zeng, L. Mei, Y. Zhao, H. Chen, *Nat. Commun.* **2023**, *14*, 6567.
[27] a) H.-Y. Tao, R.-Q. Wang, W.-J. Sheng, Y.-S. Zhen, *Int. J. Biol. Macromol.* **2021**, *187*, 24; b) Y. Zhang, T. Sun, C. Jiang, *Acta Pharm. Sin. B* **2018**, *8*, 34.
[28] C. Li, D. Zhang, Y. Pan, B. Chen, *Polymers (Basel)* **2023**, *15*, 3596.
[29] M. Lan, S. Zhao, W. Liu, C.-S. Lee, W. Zhang, P. Wang, *Adv. Healthcare Mater.* **2019**, *8*, 1900132.
[30] Z. Li, X. Lai, S. Fu, L. Ren, H. Cai, H. Zhang, Z. Gu, X. Ma, K. Luo, *Adv. Sci. (Weinh)* **2022**, *9*, 2201734.
[31] Y. T. Fan, T. J. Zhou, P. F. Cui, Y. J. He, X. Chang, L. Xing, H. L. Jiang, *Adv. Funct. Mater.* **2019**, *29*, 1806708.
[32] W. Zhang, B.-X. Yu, X.-Y. Chen, M.-Y. Yan, Q.-Q. Liu, Y.-B. Liu, N. Yang, H. Cai, N. Yan, R.-J. Kong, H. Cheng, S.-Y. Li, A. L. Chen, *Small* **2024**, *20*, 2309882.
[33] X. Qin, M. Zhang, Z. Zhao, Q. Du, Q. Li, Y. Jiang, F. Xue, Y. Luan, *Acta Biomater.* **2022**, *147*, 366.
[34] X. Feng, L. Zeng, L. Wu, Z. Chen, W. Lin, H. Song, F. Lan, *Biomed. Pharmacother.* **2024**, *178*, 117220.
[35] Y. Wang, Y. Xiang, V. W. Xin, X.-W. Wang, X.-C. Peng, X.-Q. Liu, D. Wang, N. Li, J.-T. Cheng, Y.-N. Lyv, S.-Z. Cui, Z. Ma, Q. Zhang, H.-W. Xin, *J. Hematol. Oncol.* **2020**, *13*, 107.
[36] W. Li, J. Yang, L. Luo, M. Jiang, B. Qin, H. Yin, C. Zhu, X. Yuan, J. Zhang, Z. Luo, *Nat. Commun.* **2019**, *10*, 3349.
[37] a) C. Li, P. Jiang, S. Wei, X. Xu, J. Wang, *Mol. Cancer* **2020**, *19*, 116; b) H. Raskov, A. Orhan, J. P. Christensen, I. Gögenur, *Br. J. Cancer* **2021**, *124*, 359.
[38] X. Feng, Z. Chen, Z. Liu, X. Fu, H. Song, Q. Zhang, *Int. J. Pharm.* **2023**, *639*, 122970.
[39] N. Lam, Y. Lee, D. L. Farber, *Nat. Rev. Immunol.* **2024**, *24*, 810.